CHEMISTRY OF MATERIALS

pubs.acs.org/cm

Article

[Methylhydrazinium]$_2$PbBr$_4$, a Ferroelectric Hybrid Organic–Inorganic Perovskite with Multiple Nonlinear Optical Outputs

Mirosław Mączka,* Jan K. Zaręba, Anna Gągor, Dagmara Stefańska, Maciej Ptak, Krystian Roleder, Dariusz Kajewski, Andrzej Soszyński, Katarzyna Fedoruk, and Adam Sieradzki

Cite This: https://doi.org/10.1021/acs.chemmater.0c04440

Read Online

ACCESS | Metrics & More | Article Recommendations | Supporting Information

ABSTRACT: An expansive library of structurally complex two-dimensional (2D) and three-dimensional (3D) lead halide perovskites has emerged over the past decade, finding applications in various aspects of photon management: photovoltaics, photodetection, light emission, and nonlinear optics. Needless to say, the highest degree of structural plasticity enjoys the former group, offering a rich playground for modifications of relevant optoelectronic parameters such as exciton energy. Structural tailorability is reflected in the ease of modification of the chemistry of the organic layers residing between inorganic slabs. In this vein, we show that the introduction of methylhydrazinium cation (MHy^+, $CH_3NH_2NH_2^+$) into 2D perovskite gives a material with a record low separation of the inorganic layers (8.91 Å at 300 K). Optical studies showed that MHy_2PbBr_4 features the most red-shifted excitonic absorption among all known A_2PbBr_4 compounds as well as a small exciton binding energy of 99.9 meV. MHy_2PbBr_4 crystallizes in polar $Pmn2_1$ symmetry at room emperature (phase **III**) and at 351 K undergoes a phase transition to modulated *Pmnm* phase (**II**) followed by another phase transition at 371 K to *Pmnm* phase (**I**). The ferroelectric property of room-temperature phase **III** is inferred from switching of the pyrocurrent, dielectric measurements, and optical birefringence results. MHy_2PbBr_4 exhibits multiple nonlinear optical phenomena such as second-harmonic generation, third-harmonic generation, two-photon excited luminescence, and multiphoton excited luminescence. Analysis of MHy_2PbBr_4 single-crystal luminescence spectra obtained through linear and nonlinear optical excitation pathways indicates that free exciton emission is readily probed by the ultraviolet excitation, whereas crumpled exciton emission is detected under two- and multiphoton excitation conditions. Overall, our results demonstrate that incorporation of MHy^+ into the organic layer is an emergent strategy for obtaining a 2D perovskite with polar character and multifunctional properties.

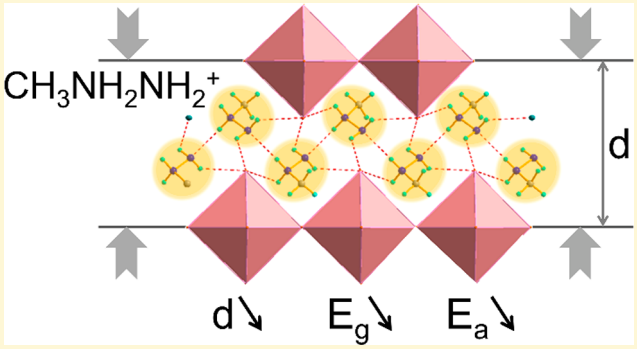

INTRODUCTION

Layered perovskites have aroused interest for a long time as a result of their ability to generate versatile molecular structures with improved stabilities and continue to exhibit unique physicochemical properties. Although the recent breakthroughs in photovoltaic technology largely revolve around modifications of archetypal 3D perovskites, it recently emerged that incorporation of 2D perovskites into photovoltaic devices can be the key to advancing further progress in the field.[1] Those high hopes stem from the fact that 2D perovskites surpass 3D counterparts in terms of higher resistance to moisture and chemical and irradiation stresses and thus can be thought of as not only active but also stability-fortifying components of photovoltaic layers.[2−4] There is also an enticing prospect for using 2D perovskites in lighting applications owing to the improved photoluminescence quantum yield (PLQY) of the bulk samples.[5]

The large diversity of available organic spacers offers enormous opportunities for tuning the structural, physical, and chemical properties of 2D perovskites.[2−5] The inorganic layers contribute to the semiconductor electronic structure; hence, due to the spatial separation, they form quantum-like structures with 2D electronic confinement.[6−9] Apart from quantum confinement, the separation of the inorganic layers by organic ones provides for the dielectric confinement of charge carriers.[7,8,10] As a result, stable excitons (electron−hole pairs) may exist at room temperature (RT).[5−11] Typically, the exciton binding energies of 2D perovskites are as high as a few hundreds of meV, which is an order of magnitude higher relative to 3D lead halide perovskites.[5−11] Unfortunately, the large exciton binding energies and wide band gaps are both responsible for the

Received: November 18, 2020
Revised: March 16, 2021

limited photovoltaic performance of the bulk 2D perovskites. Accordingly, in order to improve the optoelectronic properties of 2D perovskites, it seems pertinent to enhance the charge transport between adjacent inorganic layers and reduce the quantum well effect, which can be addressed by reducing the distance between the inorganic layers and replacing weak van der Waals interactions by stronger hydrogen bonds.[12] Here, we describe the engineering of 2D perovskites at the molecular level. One scenario is to use divalent organic cations for construction of 2D Dion–Jacobson (D–J) perovskites.[12] In the case of Ruddlesden–Popper (R–P) perovskites, small monovalent cations capable of forming multiple hydrogen bonds (HBs) can be employed to this end.[13] A promising approach reduction of the exciton binding energy is to select organic cations with high dielectric permittivity.[14,15] For instance, it was shown that lead iodide containing ethanolamine (EA) with a high dielectric permittivity of 37.7 has strongly reduced dielectric confinement and an exciton binding energy of 65 meV, as opposed to the phenylethylammonium (PEA) analogue with a dielectric constant of 3.3 and exciton binding energy of 453 meV.[15] It is also worth noting that the band gap narrows and the exciton energy decreases with decreasing octahedral tilting (crumpling of the extended corner-shared PbX_6 layers).[8,13,16,17]

In addition to photovoltaic applications, 2D hybrids are also very promising materials for light-emitting applications due to their color tunability.[4,5] Photoluminescence (PL) in lead halides usually originates from radiative recombination of excitons.[5−8,18] When these excitons migrate freely in the lattice (free excitons, FE), PL bands are narrow (full width at half-maximum, fwhm, usually less than 20 nm) and the Stokes shift is small.[5−8,17−19] However, the excitons may interact with defects (bound excitons, BE) corresponding to imperfect stacking of layers (crumpled excitons, CE) or create transient lattice deformations (self-trapped excitons, STEx).[5,8,16−22] This leads to broadening and a red shift of the PL bands.[5,8,16−22] The type of PL in 2D perovskites depends strongly on the distortion of the structure, i.e., broad PL bands with large Stokes shifts appear often for compounds exhibiting a large degree of octahedral distortion, especially for compounds with corrugated inorganic sheets, while emission of (100) perovskites is usually dominated by a narrow PL attributed to FE.[5−8,16−24] It is known that the soft lattice endows 2D perovskites with rich phase transition (PT) behavior, oftentimes originating from the dynamic disorder of the organic subframework.[7,25−27] Since the PTs usually lead to significant changes in the crumpling of the PbX_6 layers, they affect the PL and optical properties of these materials.[7,16,26,27]

Some 2D lead halides are also attractive NLO materials.[28] In the case of A_2PbBr_4 compounds, THG was reported for BA_2PbBr_4,[28] multiphoton absorption for BA_2PbBr_4 and OA_2PbBr_4,[28] and SHG for noncentrosymmetric CHA_2PbBr_4,[29] $ATHP_2PbBr_4$,[30] and BPA_2PbBr_4,[31] where BA, OA, CHA, ATH, and BPA stand for *n*-butylammonium, ocylammonium, cyclohexylammonium, 4-aminotetrahydropyran, and 3-bromopropylammonium, respectively.

Structural noncentrosymmetry of the perovskites is also a prerequisite for pyro-, piezo-, and ferroelectricity, properties essential from an applications standpoint. Generally, noncentrosymmetric 2D perovskites are not a rarity; their review is provided elsewhere.[28] On the other hand, despite a decent array of noncentrosymmetric 2D perovskites, among $n = 1$ R–J bromides ferroelectricity was reported for only three examples, i.e., CHA_2PbBr_4, $ATHP_2PbBr_4$, and very recently BPA_2PbBr_4.[29−31] It is worth adding that there is a growing demand for the discovery of novel materials possessing two or more bulk physical properties since the coexistence of different properties may lead to new types of physical phenomena when subjected to various external stimuli, enabling construction of multifunctional devices. A well-known group of such materials is multiferroics possessing the coexistence of magnetism and ferroelectricity.[32] In lead halides, combination of the ferroelectric and optoelectronic properties would lead to next-generation optoelectronic and photovoltaic devices. Among A_2PbX_4 compounds, ferroelectric $(BZA)_2PbCl_4$ (BZA = benzylammonium) and $(BA)_2PbCl_4$ were shown to exhibit narrow UV PL near 360 nm and broad-band white-light emission, respectively.[33,34] The PL properties of $ATHP_2PbBr_4$ and BPA_2PbBr_4 ferroelectrics are not known, but ferroelectric CHA_2PbBr_4 and polar BZA_2PbBr_4 were shown to exhibit broad-band white-light emission and narrow blue-violet emission, respectively.[19,35,36] Quite remarkably, the broad-band emission may be enhanced in materials crystallizing in the polar space groups because they can exhibit a much higher degree of electron–phonon coupling compared to their nonpolar analogues.[17]

Facile tunability of the physicochemical properties of 2D perovskites through structural inputs may be considered as one of primary factors promoting their intense development. This fundamental merit of 2D perovskites can be fully appreciated if one collates them with 3D counterparts. Indeed, selection of available 3D perovskite structures appears relatively narrow, as these can accommodate only a handful of cations of limited size (methylammonium, MA^+, formamidinium, FA^+, Cs^+, and recently introduced to perovskite chemistry methylhydrazinium, MHy^+)[37−43] due to the sterics imposed by the three-dimensional PbX_6 coordination net.

We now report what seems to be a useful way of obtaining polar 2D perovskites with improved optoelectronic properties, as exemplified for new member of this class, methylhydrazinium tetrabromolead(II), MHy_2PbBr_4. From a crystal engineering viewpoint, the use of MHy^+ as an organic building unit codes for the record low interlayer separation (8.91 Å at 300 K), the most red-shifted excitonic absorption among all known A_2PbBr_4 2D perovskite analogues, and a small exciton binding energy (99.9 meV) since MHy^+ embodies molecular design criteria: small molecular size, capability of multiple strong hydrogen bonds, and high-dielectric permittivity ($\varepsilon = 22$).[13,44] Moreover, in the course of our studies on the PT behavior of MHy_2PbBr_4, we discovered the ferroelectric nature of RT phase **III**. The ferroelectric property is assisted by nonlinear optical activity, as under femtosecond near-infrared excitation MHy_2PbBr_4 provides multiple nonlinear optical emissions of parametric (harmonic generation) and nonparametric (multiphoton absorption) origin. Strong two-photon excited luminescence properties of MHy_2PbBr_4 single crystals have been employed to probe the presence of CEs in a wide temperature range, which often escape detection under one-photon excitation conditions.

RESULTS AND DISCUSSION

Single-Crystal X-ray Diffraction and the Unusually Small Distance between Perovskite Layers. The crystals of MHy_2PbBr_4 adopt three temperature-controlled crystal phases. The HT phase **I** of orthorhombic *Pmnm* symmetry is centrosymmetric; phase **II**, which is stable within a narrow temperature range (ca. 15 K), accommodates the average crystal structure of phase **I** but simultaneously reveals low-intensity

https://doi.org/10.1021/acs.chemmater.0c04440
Chem. Mater. XXXX, XXX, XXX−XXX

Table 1. Distortion Parameters of MHy_2PbBr_4 Perovskite in Subsequent Polymorphic Phases[a]

phase	T (K)	Pb−Br−Pb direction[n]	θ_{tilt} (deg)	$D_{in} = 180 - \theta_{in}$ (deg)	$\Delta d \times 10^{-4}$	σ^2 (deg)
I	380	[001]	169.3(1)	10.7	2.1	11.3
		[010]	180	0		
II	360	[001]	168.8(1)	11.2	2.0	12.0
		[010]	180	0		
III	300	[001]	167.0(1)	13	2.2	18.6
		[010]	175.3(1)	4.7		
	100	[001]	162.6(1)	17.4	4.2	34.9
		[010]	172.8(1)	7.2		

[a]In all phases, $D_{out} = 180 - -\theta_{out}$ equals 0, Δd = bond length distortion; σ^2= octahedral angle variance.[45] [n]Note that directions refer to nonstandard *Pmnm* setting of *Pmmn* space group.

satellite peaks corresponding to ca. 4-fold multiplication of the *b*-lattice parameter. Accordingly, it is phase with modulated crystal structure. Phase **III** possesses the same metric as phase **I** but is polar ($Pmn2_1$ space group), thus pointing to the possibility for second-harmonic generation (SHG) and ferroelectric property.

HT phase **I** is isostructural to the previously reported HT phase of the MHy_2PbI_4 analogue.[13] Single (100) perovskite planes are separated by MHy^+ cations. It turns out that the distance between perovskite slabs is exceptionally short, i.e., 9.08 Å at 380 K, corresponding to one-half of the *a* cell parameter. *b* and *c* lattice parameters are related to intralayer Pb−Pb distances. The $PbBr_6^{4-}$ octahedra are joined by the basal Br^- ligands, so that the coordination sphere of the Pb^{2+} center consists of two apical and four bridging Br^- ions, with Pb−Br distances ranging from 2.96 to 3.09 Å. The octahedra are in-plane tilted with θ_{in} along [001] equal to 169.3(1)° (Table 1), which is very close to θ_{in} observed in MHy_2PbI_4 (170.7(1)° at 330 K).[13]

The MHy^+ are disordered over ..m mirror planes, taking two equivalent positions with equal probability. Likely due to the exceptionally short interlayer separation, the disorder is less pronounced compared to the iodine analogue for which at least three different placements for MHy^+ were observed at a much lower temperature of 330 K. Thermally induced disorder averts formation of stable intramolecular as well as N−H···Br hydrogen bonds in phase **I**. Figure 1 highlights the main structural features of phase **I** of MHy_2PbBr_4 compared with those of low-temperature (LT) phase **III**.

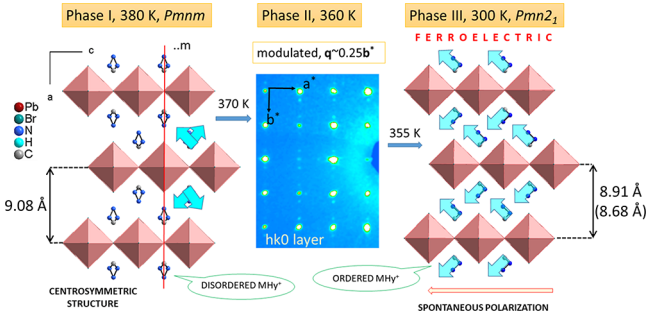

Figure 1. Projections of crystal structures of MHy_2PbBr_4 in phases **I** and **III** provided along with distances between inorganic layers separated by MHy^+ cations. In the case of phase **III**, the distance provided in brackets corresponds to the crystal structure data collected at 100 K. In the HT phase **I**, MHy^+ cations are dynamically disordered over mirror ..m planes. Temperature lowering stabilizes movements, and through modulated phase **II** the crystal structure transforms to ordered, ferroelectric phase **III**. Blue arrows denote MHy^+ dipoles.

Temperature lowering stabilizes the rotations of MHy^+. Even though the average crystal structure of phase **II** is identical to that of phase **I**, the low-intensity modulation peaks with $\mathbf{q} \approx 0.25\mathbf{b}^*$ indicate the structure alteration resulting in a notable increase of the unit cell volume ($V_{II} \approx 4V_I$). As anticipated, the interslab distance for the modulated phase **II** shortens to 9.03 Å at 360 K.

The structural PT to phase **III** leads to noncentrosymmetric, polar $Pmn2_1$ space group. Structural transformation on one hand results in the ordering of organic cations but on the other hand leads to further distortion of the perovskite layers. The resulting arrangement of MHy^+ introduces noncompensated molecular dipoles that sum up to the spontaneous polarization along the *c* direction (Figure 1). MHy^+ ions interact with each other via intermolecular N−H···N HBs and are anchored within perovskite layers via rather weak N−H···Br HBs. Apical Br^- ligands act exclusively as acceptors, and due to the symmetry restrictions (apical bromines are symmetry equivalent) the HBs are identical from both sides of the layers. The detailed geometry of the HB is given in Table S1 and Figure S1.

The observation of an unusually small distance between perovskite layers requires broader comment. Generally, the overwhelming majority of reported A_2PbBr_4 (100) perovskites contain long A^+ cations, which consistently translates into the large separation between inorganic layers. Table S2 lists the structural parameters for reported polar A_2PbBr_4 (100) perovskites and nonpolar analogues with short separation between the inorganic layers. As can be seen, the interlayer distance of MHy_2PbBr_4 (8.909 Å at RT) is very small, and the only smaller value of 8.728 Å is observed for mixed-cation $CsGAPbBr_4$ (GA stands for guanidinium), which nonetheless comprises an inorganic component.[46] Indeed, if one considers the other representatives of 2D perovskites comprising purely organic cations such as ethanolammonium (EA), ATH, BPA, BA, CHA, and benzylammonium (BZA), it is apparent that the distances between layers are equal to 9.959, 13.486, 13.6242, 13.8085, 13.999, and 16.6764 Å, respectively (Table S2).[17,19,29−31,47] The above structural data allow us to confirm our supposition that the small MHy^+ cation makes possible construction of a 2D perovskite with a record low layer separation due to the interplay of its size with the high capability for hydrogen bonding.

MHy_2PbBr_4 also shows an exceptionally small deviation of the Pb−Br−Pb angles from 180° (Table S3). A smaller D_{in} was reported only for EA_2PbBr_4, but in contrast to this compound, for which D_{out} = 6.3°, MHy_2PbBr_4 does not show any out-of-plane tilting (D_{out} = 0°, Table S2).

The foremost differences regarding changes in perovskite layers between the paraelectric phase **I** and the ferroelectric

https://doi.org/10.1021/acs.chemmater.0c04440
Chem. Mater. XXXX, XXX, XXX−XXX

phase **III** concern the interoctahedral tilting. In ferroelectric phase **III** an extra in-plane deformation along [010] arises with D_{in} equal to 7.2° (at 100 K). In addition, there is an increase in the octahedral distortion (Δd) as well as an angle variance (σ^2). Comparing to the data from paraelectric phase **I** at 380 K, at 100 K Δd doubles whereas σ^2 is almost tripled, see Table 1. Note that contrary to MHy_2PbI_4, only in-plane tilting is present in MHy_2PbBr_4 in the LT phase; furthermore, the octahedral distortion parameters and D_{in} are larger in the bromine analogue in the entire temperature range. Figure S2 shows the modifications of the perovskite layers induced by PTs in MHy_2PbBr_4.

When analyzing the changes in the crystal structure of phase **III**, the off-center displacements of the Pb^{2+} ions from the gravity center of the Br^- ligands cannot be ignored. The shifts introduce net dipoles that contribute to the polar properties of the ferroelectric phase and increase the in-plane deformations of the structure. The Pb−Br distances change along [001] from 3.21 Å at 380 K to 3.21 and 2.85 Å at 100 K. In the nonpolar [010] direction, the variations in the bridging Pb−Br bonds are much lower, see Figure S2.

Phase Transition Behavior and Determination of Polar Properties. The DSC measurements show the presence of two heat anomalies at T_1 = 371 K (368 K) and T_2 = 351 K (343 K) observed during heating (cooling) (Figure 2a and Figure S3).

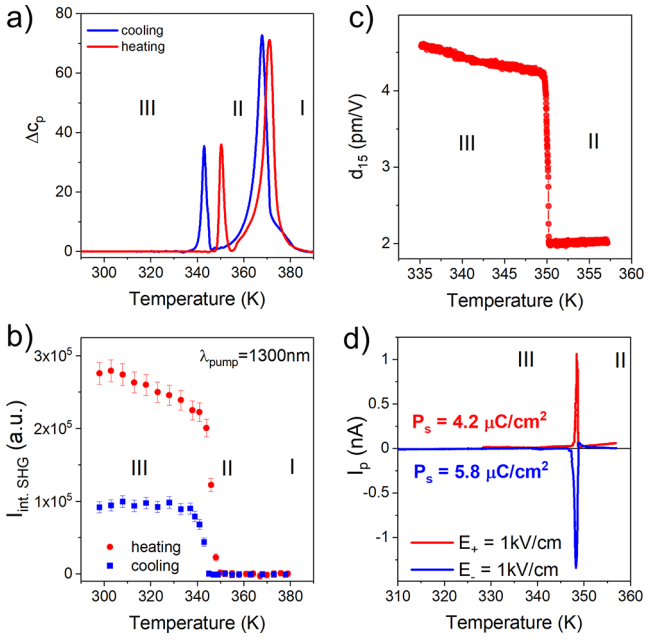

Figure 2. (a) Change in C_p related to the PT in the heating (red) and cooling (blue) runs. (b) Plots of integral intensities of the SHG signal of MHy_2PbBr_4 for heating (red circles) and cooling (blue squares) runs. (c) Temperature dependence of the piezoelectric module d_{15} observed near 350 K. (d) Changes of the pyroelectric current I_p of a single crystal in the direction of the polar axis after poling in dc electric field. E^+ and E^- are opposite directions of poling fields. I_P represents the total pyroelectric current.

The highly symmetric shapes of these anomalies, associated with sharp changes of the entropy and large thermal hysteresis all point to the first-order character of both PTs. The associated changes in the enthalpy ΔH and entropy ΔS were estimated to be ~506 J mol^{-1} and ~1.38 J mol^{-1} K^{-1} for the PT at T_1 and ~95 J mol^{-1} and ~0.28 J mol^{-1} K^{-1} for the PT at T_2 (average values). Since the X-ray diffraction data reveal 2-fold disorder in phase **I** and complete order in phase **III**, the total change in entropy is expected to be $R \ln 2$ = 5.8 J mol^{-1} K^{-1}. The experimental value of ΔS is, however, significantly smaller (1.38 + 0.28 = 1.66 J mol^{-1} K^{-1}) yet is very often reported for hybrid organic−inorganic perovskites, and it is usually attributed to the relaxor character of the studied compounds.[32,48,49] It is worth adding that the overall change of ΔS in MHy_2PbBr_4 is much smaller relative to that recently reported for the MHy_2PbI_4 analogue (~2.88 J mol^{-1} K^{-1}), which is consistent with the more pronounced disorder of the organic cations (3-fold) in the latter case.[13]

Next, TR-SHG measurements were performed to verify the symmetry of all crystal phases. Figure 2b displays plots of the integral intensities of the SHG signal ($\lambda_{max\ SHG}$ = 650 nm, integration range 610−675 nm) obtained upon MHy_2PbBr_4 irradiation with 1300 nm femtosecond laser pulses during the heating and cooling run, while Figure S4 displays the corresponding experimental spectra for the heating and cooling run. From Figure 2b it is apparent that RT phase **III** has quite strong SHG activity. One sees that upon heating, the SHG response steadily decreases up to ca. 344 K, where it exhibits a drop in its intensity; at 350 K the SHG signal is practically no longer observed. From this point onward, i.e., in the temperature range at which crystal phases **II** (351−371 K) and **I** (above 371 K) of MHy_2PbBr_4 are thermodynamically stable, the emission spectra are clearly devoid of SHG signal. Accordingly, the centrosymmetric character of these phases is confirmed by these results. On cooling from 379 to 345 K, no particular changes in the spectral characteristics are observed, but below 345 K, again in the temperature range at which phase **III** is stable, the SHG signal starts to reappear and settles at ca. 35% of its initial value. The return of SHG activity upon **II** → **III** PT attests to the reversibility of this transition.

If the phase below 350 K is of polar (ferroelectric) character, one should also observe the piezoelectric effect. To this end, strain has been measured on two separate crystals by applying the electric field perpendicular and parallel to the crystallographic *c* axis, thus allowing us to determine piezoelectric coefficients d_{15} and d_{33} in 335−357 K temperature range (Figure 2c and Figure S5, respectively). The observed sudden drop in the piezoelectric activity supports the notion that PT **II** → **I** is a first-order transition but also underlines the possibility of a ferroelectric to paraelectric nature of this PT. Note that the obtained strain response was a linear function of the electric field applied, leaving no doubt as to the piezoelectric character of the observed response (Figure S6). While the piezoelectric properties below 350 K correspond well with the observed pyroelectric properties and the nonconcentric $Pmn2_1$ group and therefore are not questioned, we may doubt whether the piezoelectric effect observed at temperatures above 350 K is of intrinsic character. In fact, the modulated structure indicated by the X-ray studies described here does not exclude the piezoelectric properties, but the fact that an electric field was used to observe piezoelectric phenomena may point to extrinsic piezoelectric properties. The lack of a SHG signal above 350 K seems to confirm this supposition.

To gain further evidence on the ferroelectricity of MHy_2PbBr_4, a study of the pyroelectric effect has been undertaken. The temperature-dependent pyrocurrent of a MHy_2PbBr_4 single crystal measured along the polar axis is presented in Figure 2d. On heating, the current increases rapidly in the vicinity of T_2. To prove that the observed pyroelectric

https://doi.org/10.1021/acs.chemmater.0c04440
Chem. Mater. XXXX, XXX, XXX−XXX

current is connected with the ferroelectric properties of the investigated crystal, the same crystal was poled in a dc electric field with reversible polarization. We observed that the pyrocurrent changes sign after poling the sample with the opposite electric field, indicating a ferroelectric behavior. Integration of the pyrocurrent allowed for estimation of the saturated value of the electric polarization, which changed from 4.6 to 5.8 $\mu C/cm^2$ for positive and negative polarized electric field, respectively. The value of P_s is similar to those found for the three known ferroelectric bromides, i.e., CHA_2PbBr_4, $ATHP_2PbBr_4$, and BPA_2PbBr_4, for which P_s was 5.8, 5.6, and 4.8 $\mu C/cm^2$, respectively.[29−31]

Thermogravimetry. Thermogravimetric data indicate that MHy_2PbBr_4 starts to decompose near 496 K (Figure S7). The weight loss between 496 and 680 K is about 39.5% and corresponds to the release of methylhydrazinium bromide (the calculated value is 40.9%). On further heating, $PbBr_2$ starts to sublimate near 800 K, and this process ends near 950 K.

Dielectric Studies. To probe the intrinsic dynamics of the title compound, dielectric spectroscopy experiments were performed on three differently oriented single-crystal samples. The highest values of dielectric permittivity changes around the PT at T_1 are observed for the sample measured along the polar axis ([001] direction). Here, one observes large lambda-like anomalies around T_1, indicating significant structural changes, which may entail changes of the internal polarization, characteristic for ferroelectric materials (Figure 3a). A slight frequency

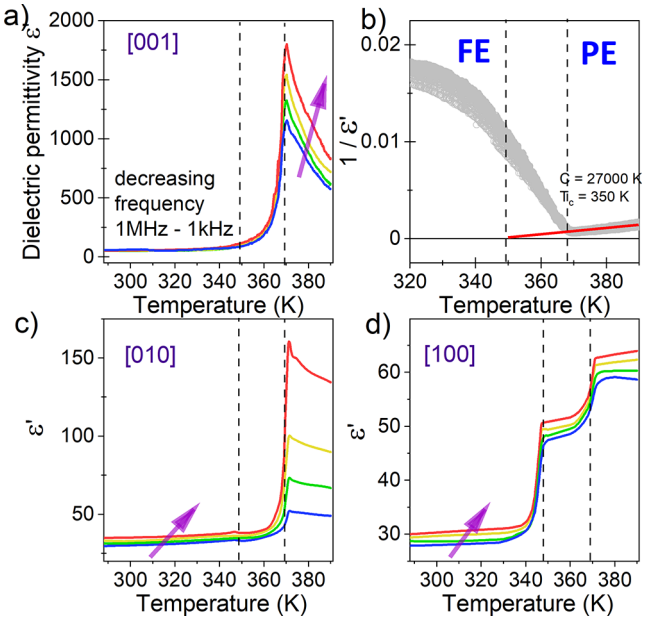

Figure 3. (a) Temperature dependence of the dielectric permittivity ε' of MHy_2PbBr_4 measured on heating along the [001] direction. (b) Curie−Weiss dependence for the sample measured along the [001] direction. (c and d) Temperature dependence of the dielectric permittivity ε' of MHy_2PbBr_4 measured along the [010] and [100] directions, respectively.

dispersion observed just above T_1, confirms a dynamic disorder in phase **I**. Surprisingly, no changes in ε' are observed for the same orientation at T_2 (Figure 3a). In order to verify ferroelectricity, the Curie−Weiss dependence was verified (Figure 3b). For all measured frequencies, the mean value of the Curie constant was 27 000 K, which is a characteristic value for classical ferroelectrics. In addition, it was observed that the Curie temperature tends to the T_2 value. This allows the conclusion that the observed PTs are from the paraelectric phase **I** to ferroelectric phase **III** via the intermediate phase **II**. Note that a similar behavior, although with much less pronounced changes of the dielectric permittivity values, was recently reported for 2D $(BA)_2(EA)_2Pb_3I_{10}$.[50]

Strong electrical anisotropy, characteristic for 2D structures, is confirmed when comparing the dielectric permittivity measurements along the [001] direction with those obtained for the [010] and [100] directions (Figure 3c and 3d). It is apparent that relative changes around T_2 are much better reflected in these data, see, e.g., changes of ε' at T_2 for sample measured along [100]. At the same time, the value of the dielectric permittivity ε' is at least of 1 order of magnitude lower in both cases compared to that measured for the [001] direction. The significant anisotropy of the dielectric permittivity of MHy_2PbBr_4 is particularly emphasized if one compares these data with results obtained for a polycrystalline pellet (Figure S8).

Optical Birefringence Measurements. The temperature evolution of the birefringence maps is shown in Figures 4, S9,

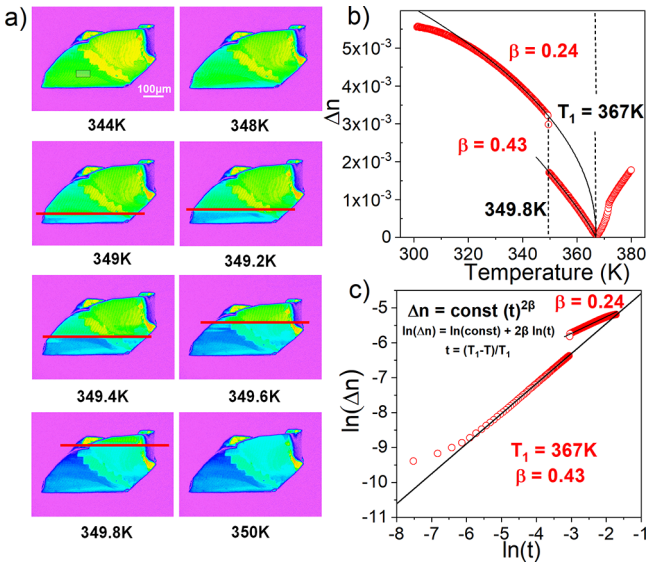

Figure 4. (a) Temperature evolution of birefringence maps near the transition at 350 K. *a* axis is perpendicular to the crystal surface, and solid line denotes the thermal front moving in the [010] direction. (b) Temperature dependence of birefringence Δn in the (b,c) plane. (c) Dependence of $\ln(\Delta n)$ versus $\ln(t)$ plotted in order to determine the exponent β.

and S10. The temperature evolution of the birefringence maps shows the appearance of a thermal front at 349 K that moves in the [010] direction on further heating (Figure 3). This front disappears at 350 K, indicating that the PT from phase **III** to phase **II** has been completed. Figure 3 also shows that the shapes of the domains do not change when passing from phase **III** to phase **II**.

Figure S10 shows the birefringence distribution in the MHy_2PbBr_4 crystal at 343 K. As can be seen, especially the left part of the crystal was in a pure single-domain state. The green parallelogram represents a region with a homogeneous distribution of birefringence. The temperature relationship of Δn obtained on heating for the (b,c) plane is presented in Figure 4b. Two characteristic temperatures have been distinguished. The first corresponds to PT between phase **III** ($Pnm2_1$

https://doi.org/10.1021/acs.chemmater.0c04440
Chem. Mater. XXXX, XXX, XXX−XXX

symmetry) and phase **II** (modulated, *Pmnm* symmetry) and the second to transition between phase **II** and phase **I** (*Pmnm* symmetry). It is interesting that in the LT phase **III** the dependence $\Delta n(T)$ can be fitted with eq 3 (see SI for details) for the same PT point equal to 367 K (see the black curves in Figure 4a and 4b). This unusual dependence would mean that the LT phase with exponent β = 0.24 behaves as if PT at 367 K corresponds to the tricritical point for which β = 0.25 is expected. However, at 349.8 K, a sharp jump of birefringence takes place and the dependence $\Delta n(T)$ is characteristic for a continuous (second-order) transition with exponent β = 0.43, very close to theoretically predicted value of 0.5. Above the transition at 367 K the phase is of orthorhombic symmetry and the birefringence is still present.

It should be noted that the domains did not change their position and size when passing PTs, both on heating and on cooling. It is a characteristic feature of the ferroelastic domains. However, observation of the pyroelectric phenomena is yet another piece of evidence that the observed domains are also ferroelectric in nature.

Linear Optical Properties. The RT diffuse reflectance spectrum shows a band at 423 nm (2.93 eV) that can be attributed to the excitonic absorption (Figure S11). Using the Kubelka–Munk relation,[51] the energy band gap (E_g) of MHy_2PbBr_4 has been estimated to be 3.02 eV (Figure S11, inset). A_2PbBr_4 layered perovskites are semiconductors with a band gap typically near 3.0 eV and with excitonic absorption in the range of 2.97–3.24 eV.[17,19,29,36,47] The energy band gap and energy of excitonic absorption of A_2PbX_4 perovskites both decrease with decreasing octahedral tilting.[8,13,16,17] Previously, the smallest value of the energy of excitonic absorption (2.97 eV) was reported for EA_2PbBr_4 (Table S2), which exhibits small octahedral tilting.[14,47] Clearly, MHy_2PbBr_4 exhibits an even smaller value of the excitonic absorption energy (2.93 eV). This behavior is consistent with a lack of out-of-plane distortion of the inorganic framework (D_{out} = 0°, compared to 6.3° for EA_2PbBr_4,[47]). It is well known that temperature-dependent studies of absorption spectra down to a few Kelvin provide information on the temperature dependence of the exciton energy and band gap as well as the exciton binding energy.[7,11] Due to strong absorption, very thin samples are needed, and they can be prepared for 2D perovskites containing large organic cations using adhesive tape.[6,7] This is possible due to the presence of weak van der Waals interactions. In the case of MHy_2PbBr_4, the inorganic layers are connected with MHy^+ cations by much stronger hydrogen bonds, and therefore, the crystals cannot be defoliated by means of adhesive tape. We report, therefore, temperature-dependent studies only on a relatively thick single crystal (Figure S12). Due to the large thickness of the crystal, we could not see exciton absorption, but the absorption spectra show narrowing of the band gap by about 67 meV in the 292–382 K range (Figure S12). The band gap shows a weak blue shift near T_2 and no clear change at T_1. This behavior is different than that usually observed at the phase transition temperatures for layered A_2PbX_4 perovskites.[7,16,26,27] For instance, studies of $(C_nH_{2n+1}NH_3)_2PbI_4$ compounds (n = 12, 16, 18) showed a large red shift (up to 20 nm) when going from the LT to HT phase attributed to a significant decrease in the crumpling of the PbI_6 layers.[27] A negligible (very weak) change of E_g for MHy_2PbBr_4 at T_1 (T_2) is consistent with a very weak (weak) change of the in-plane octahedral tilting and lack of out-of-plane tilting for all phases (see Table 1).

The photoluminescence (PL) spectrum of MHy_2PbBr_4 recorded at 80 K is dominated by the narrow (fwhm = 5 nm) PL band at 416 nm (Figure 5a). It also shows the presence of two

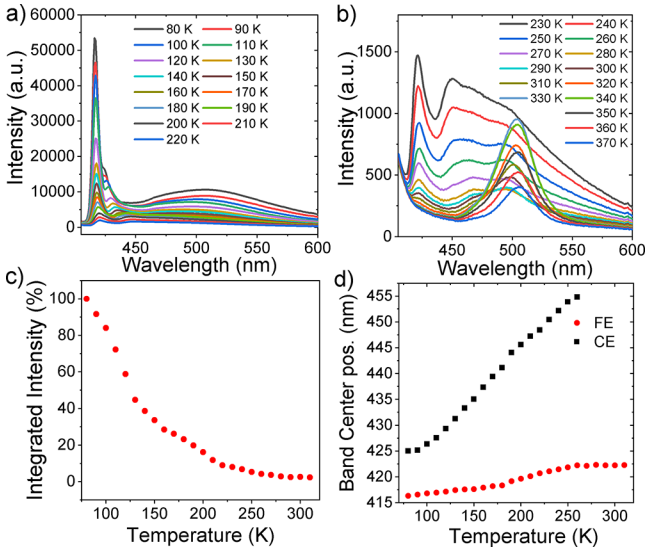

Figure 5. (a and b) Temperature-dependent PL spectra of MHy_2PbBr_4. (c) Temperature dependence of the integrated intensity for the FE band. (d) Temperature dependence of the band center positions for the FE and CE bands.

other red-shifted PL bands: a narrow band (fwhm ≈ 10 nm) at 425 nm and a very broad band (fwhm ≈160 nm) with a maximum near 507 nm. Narrow PL bands, attributed to recombination of FE from the top few near perfectly aligned layers, are typically observed for (100) lead bromide perovskites near 400 nm (Table S4).[14,17,19,20,36,46] However, PL spectra of layered perovskites often showed the presence of another narrow but weaker and red-shifted band, which was attributed to recombination of CE from the interior regions.[8,20,21] The narrow width of the 416 nm PL band of MHy_2PbBr_4, coincidence with the excitonic absorption (Figure S13), the excitation–power dependence with a slope very close to 1 (Figure S14), and a weak red shift on heating (Figure 5d) all indicate that this band originates from FE recombination. The red-shifted band at 425 nm, which exhibits a more pronounced red shift on heating (Figure 5d), can be most likely attributed to CE recombination. This assignment is also supported by analysis of MHy_2PbBr_4 luminescence spectra obtained under two- and multiphoton excitation conditions, see the Nonlinear Optical Properties section (vide infra).

By analogy with many other layered lead halide perovskites, the broad PL can be most likely attributed to the self-trapping of excitons in radiative centers. Previous studies of a number of (100) lead bromide perovskites crystallizing in centrosymmetric structures showed that such STEx-related PL exhibited a fast decrease in intensity on heating.[17,19,20,22] Furthermore, the PL intensity increased with increasing out-of-plane distortion of the inorganic layer, i.e., it was hardly visible for BA_2PbBr_4 for which D_{out} = 2.8° but was strong for $HISPbBr_4$ (HIS stands for histaminium) for which D_{out} = 22.8°.[17] A similar PL was also observed for one R–P and many D–J polar (100) lead bromide perovskites, and it was argued that the intensity of the broad PL is enhanced compared to the centrosymmetric analogues.[35,52–54] As a result, a broad PL band at ~620 nm was observed for CHA_2PbBr_4, even though this perovskite shows no

https://doi.org/10.1021/acs.chemmater.0c04440
Chem. Mater. XXXX, XXX, XXX–XXX

out-of-plane distortion.[35,52] This behavior was attributed to a higher degree of electron−phonon coupling in polar materials.[17] It is worth noting, however, that another polar perovskite, BZA_2PbBr_4, shows a narrow PL band (Table S2),[36] and ferroelectric MHy_2PbBr_4 studied here exhibits a narrow and broad PL. Thus, the polar properties alone cannot explain the pronounced differences between the PL of CHA_2PbBr_4, BZA_2PbBr_4, and MHy_2PbBr_4. Inspection of Table S2 shows, however, that CHA_2PbBr_4 has very large octahedral distortion ($\Delta d = 69 \times 10^{-5}$) and angle variance ($\sigma^2 = 27°$), BZA_2PbBr_4 has nearly regular $PbBr_6$ octahedra ($\Delta d = 1 \times 10^{-5}$ and $\sigma^2 = 0°$), and the values of Δd (22×10^{-5}) and σ^2 (18.6°) for MHy_2PbBr_4 are intermediate between those reported for CHA_2PbBr_4 and BZA_2PbBr_4. Thus, the different PL properties of these compounds seem to be related to differences in octahedral distortion.

When the temperature increases, the intensity of the broad PL band strongly decreases. Above 250 K, a new narrower (fwhm ≈ 37 nm) asymmetric band appears near 500 nm. The intensity of this band increases when the temperature increases from 290 to 330 K and decreases on further heating. Figure S15 shows that when the sample heat treated to 370 K is cooled back to 200 and 80 K, the narrow FE PL band becomes again very clearly observed but the strongly red-shifted PL dominates. Thus, this new PL arises from carriers trapped at light-induced permanent defects.

The PLQY of MHy_2PbBr_4 reaches 0.7% at RT. This value is typical for 2D lead bromide perovskites but is significantly smaller than 3.37% reported for highly efficient white-light-emitting $(2meptH_2)PbBr_4$ (2mept stands for 2-methyl-1,5-diaminopentane).[54]

Figure 5c shows that the intensity of the FE PL exhibits a strong temperature dependence. The temperature dependence of the PL intensity can be written as

$$I(T) = \frac{I_0}{1 + Ae^{-E_a/k_BT}}$$

where I_0, E_a, and k_B correspond to the emission intensity at low temperature, the activation energy, and the Boltzmann constant, respectively. After taking the natural logarithm, the formula can be rewritten as

$$\ln\left(\frac{I_0}{I(T)} - 1\right) = \ln A - \frac{E_a}{k_BT}$$

Figure S16 shows that $\ln(I_0/I(T) - 1)$ is a linear function of $1/k_BT$. Thus, using a linear fit, the activation energy for thermal quenching (often assumed to be related to the exciton binding energy[11,15]) is estimated to be 99.9 meV (Figure S16). This value is higher than that for the MHy_2PbI_4 analogue, for which E_a = 59.2 meV,[13] but much lower than those typically observed for A_2PbBr_4 compounds comprising bulky A^+ cations (above 300 meV).[5,15] In a similar manner to the MHy_2PbI_4 analogue, this behavior can be attributed to the short separation between inorganic layers and the large dielectric constant of the MHy^+ cations that significantly reduces dielectric confinement and the exciton binding energy.

The PL of MHy_2PbBr_4 is greenish blue at 80 K under 375 nm excitation with CIE coordinates (0.242, 0.314) (Figure S17). We find that MHy_2PbBr_4 is thermochromic, i.e., the color of the PL changes with increasing temperature to bluish green.

To further understand the origin of the PL bands, we also performed femtosecond time-resolved measurements under a 375 nm excitation line generated by the femtosecond laser (Figure S18). The lifetimes of the 416, 426, and 500 nm emissions are 0.54, 0.44, and 1.08 ns, respectively. The lifetimes are shorter than those reported for the wide-band white emission of $(2meptH_2)PbBr_4$ (2.23 ns) but longer than those of MHy_2PbI_4 (0.37 ns at 560 nm and 0.46 ns 573 nm).[13,54]

Nonlinear Optical Properties. TR-SHG measurements showed that phase **III** generates a second harmonic of radiation (Figure 2b). To get a quantitative measure of the SHG response of MHy_2PbBr_4 at RT, the Kurtz−Perry powder test was performed[55] using microcrystalline KDP powder as a reference (Figure S19). We found that 2D MHy_2PbBr_4 produces SHG as strong as 0.10 times that of KDP. By comparison, the recently described 3D perovskite $MHyPbBr_3$ offered a SHG response as high as 0.18 times that of KDP at the same excitation wavelength.[43] Although the SHG produced by MHy_2PbBr_4 is roughly two times lower than that of $MHyPbBr_3$, of particular note is the fact that it constitutes a new example of a lead halide perovskite material that features a noncentrosymmetric lattice at RT. On this point it should be added that apart from 3D $MHyPbX_3$ (X = Br, Cl) and 2D MHy_2PbBr_4 described here, there are several more lead halide perovskites for which noncentrosymmetry is proven with the SHG technique, e.g., bromides CHA_2PbBr_4,[29] $ATHP_2PbBr_4$,[30] and BPA_2PbBr_4,[31] as well as $(BZA)_2PbCl_4$,[33] $(CH_3(CH_2)_3NH_3)_2(CH_3NH_3)_{n-1}Pb_nI_{3n+1}$ (n = 1, 2, 3, 4, ∞),[56] or $(PEA)_2(MA)_{n-1}Pb_nI_{3n+1}$ (PEA stands for phenylethylammonium).[57]

Closer examination of the data plotted in Figure 6a reveals that spectra collected up to ca. 345 K (phase **III**), apart from the SHG signal, contain two additional emissions peaking at 433 and

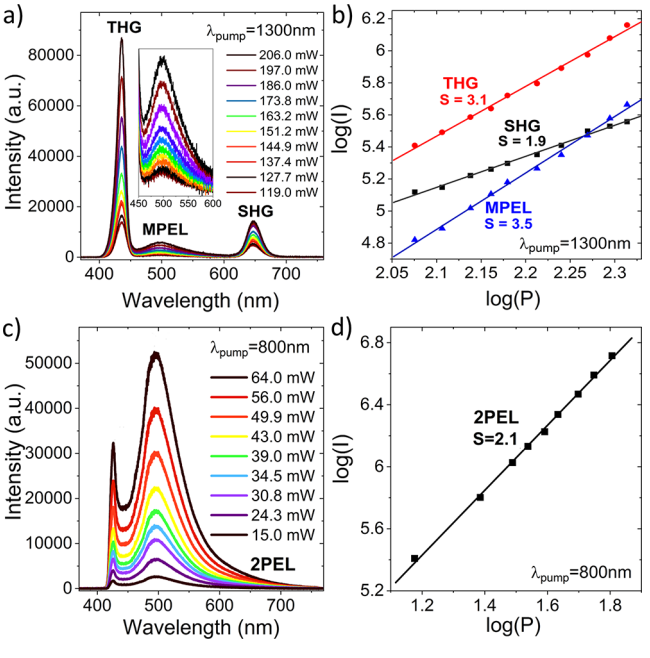

Figure 6. (a) Emission spectra of MHy_2PbBr_4 single crystals collected as a function of the applied laser power (λ_{pump} = 1300 nm) at 80 K. (b) log−log plots of integral intensities of emissions of various nonlinear optical origins (SHG, THG, and MPEL) as a function of applied laser power. (c) 2PEL emission spectra of MHy_2PbBr_4 single crystals measured as a function of the applied laser power (λ_{pump} = 800 nm) collected at 80 K. (d) log−log plot of integral intensities 2PEL emissions as a function of applied laser power for MHy_2PbBr_4.

https://doi.org/10.1021/acs.chemmater.0c04440
Chem. Mater. XXXX, XXX, XXX−XXX

500 nm, the presence of which calls for broader comment. The former one is a THG (third harmonic generation) response, while the latter feature, whose emission envelope resembles those obtained under one-photon excitation conditions (Figure 5), corresponds to the multiphoton excited luminescence of MHy_2PbBr_4. To establish the actual nature of this emission, a power-dependent luminescence experiment was performed at 80 K on a single crystal. In Figure 6a are presented experimental spectra for different excitation powers obtained at a pumping wavelength of 1300 nm, while Figure 6b displays the corresponding $\log(I) = f(\log(P))$ plots with least-squares linear fits for all registered emissions. It turns out that the slope of the linear fit characterizing the emission centered at 500 nm is equal to 3.5, indicating that, most likely, both three-photon and four-photon absorptions participate in the observed luminescence signal (in Figure 6 referred to as MPEL, multiphoton excited luminescence). Slopes of the linear fits for the SHG and THG emissions are almost equal to the anticipated values of 2 and 3, but more critically, they serve as internal standards that validate our results regarding the determination of simultaneous 3PEL and 4PEL for MHy_2PbBr_4 at 1300 nm. This observation is in accordance with a recent report by Chen et al., who discovered multiphoton absorption in nanoparticles based on $MAPbBr_3$, $MAPbBr_3/(OA)_2PbBr_4$, and $CsPbBr_3$ lead perovskite matrices (where MA and OA stand for methylamine and oleic acid, respectively), the nature of which was three, four and even five photon depending on the excitation wavelength.[58]

The power-dependent PL experiment performed at 80 K for the MHy_2PbBr_4 single crystal (Figure 6c and 6d) clearly shows that upconverted luminescence excited at 800 nm has a two-photon origin. Note that there is no visible SHG signal at 400 nm in the emission spectra (Figure 6c) due to strong self-absorption of the second harmonic of radiation. Closer inspection of the luminescence spectra for the MHy_2PbBr_4 single crystal cooled to 80 K (Figure 6c) reveals that emissions obtained under two-photon excitation conditions (800 nm) contain the same component of broad emission (centered at 500 nm, ascribed to STEx) as found in one-photon excited spectra (Figure 5). More importantly, spectra obtained under different excitation modes clearly differ in the position of the narrow emission band. Specifically, the two-photon excitation leads to a strong luminescence peak at 425 nm and no emission at 416 nm, while ultraviolet excitation (375 nm) gives rise to a strong narrow emission at a shorter wavelength −416 nm and a weak band at 425 nm. Recent spectroscopic studies of 2D hybrid perovskites demonstrate that linear excitation probes predominantly free excitons (FE), i.e., excitons that originate from only a few outer perovskite layers.[20,21] The shallow penetration depth of linear excitation is due to rapid attenuation of the excitation that takes place once it enters the crystal depth. By contrast, sub-band-gap excitation (two-photon or multiphoton), typically in the near-infrared region, is negligibly attenuated by one-photon absorption bands; hence, it reaches much deeper regions of the investigated crystal. Therefore, the excitation that proceeds via nonlinear absorption probes CE which are associated with structural deformations of inorganic layers.[20,21] Thus, the obtained results lend support to the CE character of the luminescence peak at 425 nm registered at 80 K.

However, we sought to confirm the CE nature of the emission peak in question by performing the temperature-resolved experiment. By varying the temperature from 80 to 370 K, we monitored the two-photon excited emission spectra of single-crystalline MHy_2PbBr_4. Collected spectra are provided in Figure S20. As expected, with increasing temperature one notes that the CE emission peak broadens, progressively subsides, as well as shifts to higher wavelengths. It should be also stressed that CE emission can still be seen at 316 K. Beyond that temperature point the overall luminescence efficiency is very weak due to thermal relaxation; apart from that, the CE emission itself is significantly thermally broadened and escapes detection, so that no observation can be made as to the specific behavior of CE when the temperature crosses through **III** → **II** and **II** → **I** PTs. We also note the analogous temperature-resolved experiments we performed by irradiation of a MHy_2PbBr_4 single crystal with the use of 1000 and 1300 nm femtosecond laser pulses. At 1000 nm, where also 2PA occurs yet with some contribution of 3PA (Figure S21), the obtained temperature-resolved set of spectra is similar to that for 800 nm (Figure S22 in SI), although the CE emission is less clearly marked. Indeed, at 295 K, the CE luminescence signal can no longer be seen. The temperature-resolved study at 1300 nm shows that the CE emission is significantly overlapped by THG (433 nm) of the fundamental beam, which makes monitoring the temperature evolution of the CE emission at this wavelength ineffective (Figure S23). In addition, we observed that in order to register the MPEL signal with a good signal-to-noise ratio, much higher laser fluences had to be used compared to 800 nm excitation, which led to noticeable photobleaching of the sample, yet still less than under 375 nm excitation (see the previous paragraph). Thus, based on this experience, we suggest that using 3PEL or 4PEL for temperature-dependent studies of exciton luminescence demands a high intrinsic stability of the sample; also, the possibility of overlapping parametric and nonparametric emissions has to be taken into account beforehand.

MHy_2PbBr_4 was also investigated to see how its nonlinear absorption properties, measured at 800 nm, compare to those recently determined for $MHyPbBr_3$ perovskite.[43] Measurement of the two-photon brightness, $\sigma_2\varphi$, was performed at RT on a powdered sample of MHy_2PbBr_4 using the solid-state two-photon excited fluorescence (SSTPEF) technique using bis(4-diphenylamino)stilbene (BDPAS) as a reference compound.[59] It is found that the $\sigma_2\varphi$ value at 800 nm is equal to 13 GM per MHy_2PbBr_4 structural unit. Assuming that the PL quantum yield (PLQY) of MHy_2PbBr_4 bulk sample is not higher than 1%, we find the value of the two-photon absorption cross section σ_2 is not lower than 1300 GM, also calculated per MHy_2PbBr_4 structural unit.

Various scaling methods can be used for obtaining more telling comparisons of the two-photon absorption efficiency between disparate materials. Among them, the molar mass normalized σ_2/M figure-of-merit can be considered as one of the most convenient since it allows for facile comparisons of the nonlinear response between objects of different chemical nature.[60,61] In the case of MHy_2PbBr_4, the molecular weight of the chemical formula was used for the scaling procedure. By doing so, the σ_2/M value for 2D MHy_2PbBr_4 is found to be equal to 2.1 GM·mol·g^{-1} (M = 620.98 g·mol^{-1}). This value is smaller than that for 3D $MHyPbBr_3$ (3.90 GM·mol·g^{-1}) yet generally falls into the range of σ_2/M values recently determined as typical for 3D lead bromide perovskite materials (0.6−11.7 GM·mol·g^{-1}).[43] Noteworthy, the high σ_2/M values are of the same order as those determined for plasmonic nanoobjects (e.g., 10 nm × 35 nm gold nanorods σ_{2max}/M = 7.50 at 530 nm,[62] 10 nm thick gold nanoshells, σ_{2max}/M = 2.56 at 600 nm[63]), which are regarded as one of the strongest two-photon absorbers.

https://doi.org/10.1021/acs.chemmater.0c04440
Chem. Mater. XXXX, XXX, XXX−XXX

CONCLUSIONS

The importance of 2D perovskites is very wide ranging and extends to energy conversion; hence, finding effective ways to tune their optoelectronic properties is of paramount importance. Here, we reported the discovery of 2D lead bromide MHy_2PbBr_4 comprising a small, highly hydrogen-bonded MHy^+ cation with high dielectric permittivity. The gathered data demonstrate that MHy_2PbBr_4 has a very small interlayer separation of 8.91 Å as identified for phase **III** at 300 K and the most red-shifted excitonic absorption among all known A_2PbBr_4 (100) compounds. It also has a small energy activation for thermal quenching (99.9 meV) that might indicate a low exciton binding energy. However, further temperature-dependent absorption studies are needed to estimate precisely the excition binding energy. Structurally, MHy_2PbBr_4 crystallizes as noncentrosymmetric $Pmn2_1$ phase **III** below 351 K, centrosymmetric *Pmnm* phase **I** above 371 K, and modulated *Pmnm* phase **II** in the 351−371 K range. Electrical studies provided strong evidence that phase **III** is ferroelectric and piezoelectric. MHy_2PbBr_4 exhibits a greenish blue PL under 375 nm excitation dominated by a PL band at 416 nm attributed to FE recombination. Under femtosecond near-infrared excitation, it provides disparate emissions comprising parametric (SHG, THG) and nonparametric (2PEL and MPEL) nonlinear optical processes. Temperature-resolved 2PEL and MPEL studies of MHy_2PbBr_4 indicate that emission spectra are completely devoid of a sharp peak at 416 nm but contain a strong narrow emission at 425 nm. This finding implies the presence of structural distortions that give rise to CEs and associated with them emissions. An 800 nm femtosecond laser excitation was the most effective for CE monitoring in terms of signal strength (particularly CE component) and sample stability. While we successfully detected CE emission through 3PA/4PA excitation at 1300 nm, the high laser intensity required for multiphoton excitation leads to deleterious photogeneration of defects, let alone the convolution of the MPEL with parametric signals that makes spectral analysis much less convenient.

The coexistence of noncentrosymmetry-related electrical phenomena such as ferroelectricity and nonlinear optical energy upconversion provides a unique blend of functional properties desirable in a myriad of applications.

METHODS

Synthesis. $PbBr_2$ (98%, Sigma-Aldrich), methylhydrazine (98%, Sigma-Aldrich), hydrobromic acid (48 wt % in H_2O, Sigma-Aldrich), methyl acetate (99.5%, Sigma-Aldrich), and *N*,*N*-dimethylformamide (DMF, 99.8%) were commercially available and used without further purification. In order to grow single crystals, HBr was added dropwise to 11 mmol of methylhydrazine until pH = 7. Then 5 mmol of $PbBr_2$ was added, and the mixture was stirred for 0.5 h. Since after this time not all of $PbBr_2$ was dissolved, DMF (about 2 mL) was added dropwise until complete dissolution of $PbBr_2$. The solution was filtered and placed in a glass vial, and this vial was placed in a second larger glass vial containing methyl acetate. The lid of the outer vial was thoroughly sealed, whereas the lid of the inner vial was loosened to allow diffusion of methyl acetate into the precursor solution. Colorless transparent crystals with dimensions up to 20 mm (Figure S24) were harvested after 4 days, filtered from the mother liquid, and dried at RT. A good match of their powder XRD patterns with the calculated ones based on single-crystal data (Figure S25) confirmed the phase purity of the bulk sample.

Single-Crystal X-ray Diffraction. Single-crystal X-ray diffraction was collected on a Xcalibur Atlas diffractometer operating with Mo Kα radiation. The open-flow cooling system (Oxford Diffraction) maintained nonambient temperatures. The data were processed in CrysAlisPro and CrysAlisRed software (Rigaku OD, 2015). Crystal structures were solved and refined using SHELXT 2014/5 and SHELXL2018/3.[64] Details concerning the crystals, data collection, and refinement are given in Table S4. Due to pronounced disorder in the high temperature in Phase **I**, the positions of the hydrogen atoms from the terminal NH_2 groups were not localized. In Phase **II**, only the average crystal structure is provided. The presence of additional satellite peaks marks the structure modulation with modulation vector **q** close to 1/4**b***. Nevertheless, due to the very weak intensity of these additional reflections, the modulated structure was not solved.

DSC and Thermogravimetric (TGA) Measurements. Heat capacity was measured using a Mettler Toledo DSC-1 calorimeter with a high resolution of 0.4 μW. Nitrogen was used as a purging gas, and the heating and cooling rate was 5 K/min. The sample weight was 67.42 mg. The excess heat capacity associated with the PTs was evaluated by subtraction from the data the baseline representing variation in the absence of the PTs. TGA study was performed in the temperature range 300−1123 K using a PerkinElmer TGA 4000. The sample weight was ca. 16.95 mg, and the heating speed rate was 10 K/min. Pure nitrogen gas as an atmosphere was used.

X-ray Powder Diffraction. The powder XRD pattern was obtained on an X'Pert PRO X-ray diffraction system equipped with a PIXcel ultrafast line detector and Soller slits for Cu Kα_1 radiation (λ = 1.54056 Å). The powdered sample was measured in the reflection mode, and the X-ray tube settings were 30 mA and 40 kV.

Measurements of Optical Birefringence. The Metripol system consists of a polarizing microscope equipped with a computer-controlled plane polarizer capable of being rotated to fixed angles α from a reference position, a circularly polarizing analyzer, and a CCD camera. Closer details of the Metripol setup are described elsewhere.[65,66] The crystal was heated in a high-precision Linkam THMSG 600 temperature stage. The hot stage was capable of maintaining a constant temperature to within 0.1 K, and the temperature ramps were performed at a rate of 0.4 K min^{-1}. Additional details are provided in the SI.

Dielectric, Pyroelectric and Piezoelectric Measurements. The dielectric measurements at ambient pressure were performed on single-crystal samples along the [100], [010], and [011] crystallographic directions using a Novocontrol Alpha impedance analyzer. For comparison, the polycrystalline pellet sample was prepared with a diameter of 5 mm and thickness of 0.8 mm. Samples were dried, and the silver paste was used to ensure good electrical contact. An alternating current voltage with an amplitude of 1 V and frequency in the range 10^2−10^6 Hz was applied across the samples. The temperature was controlled by the Novo-Control Quattro system using a nitrogen gas cryostat. The measurements were collected every 0.5 K/min in the temperature range from 290 to 390 K. The temperature stability of the samples was better than 0.1 K.

The pyroelectric measurements were conducted on a virgin crystal, not subjected to temperature cycles. To avoid dielectric breakdown, an electric field of 1 kV/cm strength was applied on cooling from 330 K to room temperature. The pyroelectric current of the sample was registered by means of a Keithley 6514 System Electrometer on heating with a constant rate of 1 K/min.

A quasi-static method based on a capacitance sensor was used to determine the piezoelectric strain η in the crystal under an applied electric field. Details of the measurement method using a reverse piezoelectric effect, can be found elsewhere.[67] Sample deformation was induced by an alternating electric field E of frequency 160 Hz applied to the sample and transferred via a quartz rod with one end placed on the sample surface and the second one connected to the plate of the capacitor sensor C_0. The value of C_0 was adjustable to optimize the resolution depending on the magnitude of the strain being measured. The surface area of the end of the quartz rod touching the crystal was on the order of dozens of μm^2. Additional details are provided in the SI.

One-Photon Absorption and Photoluminescence Studies. The RT diffuse reflectance spectrum of the powdered sample was measured using a Varian Cary 5E UV−vis-NIR spectrophotometer. Temperature-dependent emission spectra under 375 nm excitation from a diode laser were measured with the Hamamatsu photonic multichannel analyzer PMA-12 equipped with a BT-CCD linear image

https://doi.org/10.1021/acs.chemmater.0c04440
Chem. Mater. XXXX, XXX, XXX−XXX

sensor. The temperature of the single-crystal sample was controlled using a Linkam THMS 600 Heating/Freezing Stage. Quantum efficiency was measured on Hamamatsu Absolute PL quantum yield measurement system C9920-02G. To record time-resolved PL spectra and decay times, a femtosecond laser (Coherent Model Libra) was used as an excitation source (λ_{exc} = 375 nm).

Nonlinear Optical Properties. SSTPEF and TR-SHG studies were performed using a laser system consisting of a Quantronix Integra-C regenerative amplifier operating as an 800 nm pump and a Quantronix-Palitra-FS BIBO crystal-based optical parametric amplifier (OPA). This system delivers wavelength-tunable pulses of ∼130 fs length and operates at a repetition rate of 1 kHz. TR-SHG measurements have been performed using the 1300 nm output from the Quantronix-Palitra-FS OPA, whereas for SSTPEF measurements direct output from the regenerative amplifier was employed. Temperature-resolved 2PEL and MPEL experiments on single crystals have been performed using a laser system consisting of a Coherent Astrella Ti:sapphire regenerative amplifier providing 800 nm pulses (75 fs pulse duration, 1 kHz repetition rate) driving a wavelength-tunable TOPAS Prime OPA. Temperature control of the single-crystal sample was performed using a Linkam LTS420 Heating/Freezing Stage. Additional details are provided in the SI.

■ ASSOCIATED CONTENT

Supporting Information

The Supporting Information is available free of charge at https://pubs.acs.org/doi/10.1021/acs.chemmater.0c04440.

Additional descriptions of experiments, hydrogen-bond parameters for the studied compound at different temperatures, structural and optical parameters for selected A_2PbBr_4 (100) perovskites, crystal data, projections of crystal structures, DSC traces, NLO spectra, piezoelectric characterization, TGA plot, dielectric permittivity of a pellet, birefringence maps, diffuse reflectance spectrum, temperature-dependent absorption spectra, PL plots, power dependence of PL, CIE coordinates, temperature-dependent decay times, SHG spectra, emission spectra under 800, 1000, and 1300 nm excitation, photo of the single crystal (PDF)

CIF file for the structure of MHy_2PbBr_4 at 380 K (CIF)

CIF file for the structure of MHy_2PbBr_4 at 360 K (CIF)

CIF file for the structure of MHy_2PbBr_4 at 300 K (CIF)

CIF file for the structure of MHy_2PbBr_4 at 100 K (CIF)

■ AUTHOR INFORMATION

Corresponding Author

Mirosław Mączka − *Institute of Low Temperature and Structure Research, Polish Academy of Sciences, 50-422 Wrocław, Poland;* orcid.org/0000-0003-2978-1093; Phone: +48-713954161; Email: m.maczka@int.pan.wroc.pl; Fax: +48-713441029

Authors

Jan K. Zaręba − *Advanced Materials Engineering and Modeling Group, Wrocław University of Science and Technology, 50-370 Wrocław, Poland;* orcid.org/0000-0001-6117-6876

Anna Gągor − *Institute of Low Temperature and Structure Research, Polish Academy of Sciences, 50-422 Wrocław, Poland*

Dagmara Stefańska − *Institute of Low Temperature and Structure Research, Polish Academy of Sciences, 50-422 Wrocław, Poland;* orcid.org/0000-0002-1051-3761

Maciej Ptak − *Institute of Low Temperature and Structure Research, Polish Academy of Sciences, 50-422 Wrocław, Poland;* orcid.org/0000-0002-4639-2367

Krystian Roleder − *Institute of Physics, University of Silesia, 41-500 Chorzów, Poland*

Dariusz Kajewski − *Institute of Physics, University of Silesia, 41-500 Chorzów, Poland*

Andrzej Soszyński − *Institute of Physics, University of Silesia, 41-500 Chorzów, Poland*

Katarzyna Fedoruk − *Department of Experimental Physics, Wrocław University of Science and Technology, 50-370 Wrocław, Poland*

Adam Sieradzki − *Department of Experimental Physics, Wrocław University of Science and Technology, 50-370 Wrocław, Poland;* orcid.org/0000-0003-4136-5754

Complete contact information is available at: https://pubs.acs.org/10.1021/acs.chemmater.0c04440

Author Contributions

The manuscript was written through contributions of all authors. All authors have given approval to the final version of the manuscript.

Notes

The authors declare no competing financial interest.

■ ACKNOWLEDGMENTS

This research was supported by the National Science Center (Narodowe Centrum Nauki) in Poland under project No. 2019/35/B/ST5/00043. J.K.Z. acknowledges financial support from the Wroclaw University of Science and Technology.

■ REFERENCES

(1) Gao, X.; Zhang, X.; Yin, W.; Wang, H.; Hu, Y.; Zhang, Q.; Shi, Z.; Colvin, V. L.; Yu, W. W.; Zhang, Y. Ruddlesden-Popper Perovskites: Synthesis and Optical Properties for Optoelectronic Applications. *Adv. Sci.* **2019**, *6* (22), 1900941.

(2) Huo, C.; Cai, B.; Yuan, Z.; Ma, B.; Zeng, H. Two-Dimensional Metal Halide Perovskites: Theory, Synthesis, and Optoelectronics. *Small Methods* **2017**, *1* (3), 1600018.

(3) Chao, L.; Wang, Z.; Xia, Y.; Chen, Y.; Huang, W. Recent Progress on Low Dimensional Perovskite Solar Cells. *J. Energy Chem.* **2018**, *27* (4), 1091−1100.

(4) Quan, L. N.; Rand, B. P.; Friend, R. H.; Mhaisalkar, S. G.; Lee, T.-W.; Sargent, E. H. Perovskites for Next-Generation Optical Sources. *Chem. Rev.* **2019**, *119* (12), 7444−7477.

(5) Smith, M. D.; Connor, B. A.; Karunadasa, H. I. Tuning the Luminescence of Layered Halide Perovskites. *Chem. Rev.* **2019**, *119* (5), 3104−3139.

(6) Ishihara, T.; Takahashi, J.; Goto, T. Exciton State in Two-Dimensional Perovskite Semiconductor $(C_{10}H_{21}NH_3)_2PbI_4$. *Solid State Commun.* **1989**, *69* (9), 933−936.

(7) Ishihara, T. Optical Properties of PbI-based Perovskite Structures. *J. Lumin.* **1994**, *60-61*, 269−274.

(8) Pradeesh, K.; Nageswara Rao, K.; Vijaya Prakash, G. Synthesis, Structural, Thermal and Optical Studies of Organic-Inorganic Hybrid Semiconductors, R-PbI_4. *J. Appl. Phys.* **2013**, *113*, 083523.

(9) Chong, W. K.; Thirumal, K.; Giovanni, D.; Goh, T. W.; Liu, X.; Mathews, N.; Mhaisalkar, S.; Sum, T. C. Dominant Factors Limiting the Optical Gain in Layered Two-Dimensional Halide Perovskite Thin Films. *Phys. Chem. Chem. Phys.* **2016**, *18* (21), 14701−14708.

(10) Hong, X.; Ishihara, T.; Nurmikko, A. V. Dielectric Confinement Effect on Excitons in PbI4-Based Layered Semiconductors. *Phys. Rev. B: Condens. Matter Mater. Phys.* **1992**, *45* (12), 6961−6964.

(11) Ishihara, T.; Takahashi, J.; Goto, T. Optical Properties due to Electronic Transitions in Tow-Dimensional Semiconductors $(C_nH_{2n+1}NH_3)_2PbI_4$. *Phys. Rev. B: Condens. Matter Mater. Phys.* **1990**, *42* (17), 11099−11107.

(12) Xu, Z.; Chen, M.; Liu, S. F. First-Principles Study of Enhanced Out-of-Plane Transport Properties and Stability in Dion-Jacobson Two-Dimensional Perovskite Semiconductors for High-Performance Solar Cell Applications. *J. Phys. Chem. Lett.* **2019**, *10*, 3670−3675.
(13) Mączka, M.; Ptak, M.; Gągor, A.; Stefańska, D.; Sieradzki, A. Layered Lead Iodide of $[Methylhydrazinium]_2PbI_4$ with a Reduced Band Gap: Thermochromic Luminescence and Switchable Dielectric Properties Triggered by Structural Phase Transitions. *Chem. Mater.* **2019**, *31* (20), 8563−8575.
(14) Cheng, B.; Li, T.-Y.; Maity, P.; Wei, P.-C.; Nordlund, D.; Ho, K.-T.; Lien, D.-H.; Lin, C.-H.; Liang, R.-Z.; Miao, X.; Ajia, I. A.; Yin, J.; Sokaras, D.; Javey, A.; Roqan, I. S.; Mohammed, O. F.; He, J.-H. Extremely Reduced Dielectric Confinement in Two-Dimensional Hybrid Perovskites with Large Polar Organics. *Commun. Phys.* **2018**, *1* (1), 80.
(15) Chakraborty, R.; Nag, A. Correlation of Dielectric Confinement and Excitonic Binding Energy in 2D Layered Hybrid Perovskites Using Temperature Dependent Photoluminescence. *J. Phys. Chem. C* **2020**, *124* (29), 16177−16185.
(16) Pradeesh, K.; Baumberg, J. J.; Prakash, G. V. Exciton Switching and Peierls Transitions in Hybrid Organic-Inorganic Self-Assembled Quantum Wells. *Appl. Phys. Lett.* **2009**, *95*, 173305.
(17) Smith, M. D.; Jaffe, A.; Dohner, E. R.; Lindenberg, A. M.; Karunadasa, H. I. Structural Origins of Broadband Emission from Layered Pb-Br Hybrid Perovskites. *Chem. Sci.* **2017**, *8* (6), 4497−4504.
(18) Lekina, Y.; Shen, Z. X. Excitonic States and Structural Stability in Two-Dimensional Hybrid Organic-Inorganic Perovskites. *J. Sci.: Adv. Mater. Devices* **2019**, *4*, 189−200.
(19) Du, K.-Z.; Tu, Q.; Zhang, X.; Han, Q.; Liu, J.; Zauscher, S.; Mitzi, D. B. Two-Dimensional Lead(II) Halide-Based Hybrid Perovskites Templated by Acene Alkylamines: Crystal Structures, Optical Properties and Piezoelectricity. *Inorg. Chem.* **2017**, *56*, 9291−9302.
(20) Adnan, M.; Rao, K. N.; Acharyya, J. N.; Kumar, D.; Dehury, K. M.; Prakash, G. V. Synthesis, Structural, Linear and Nonlinear Optical Studies of Inorganic-Organic Hybrid Semiconductors $(R\text{-}C_6H_4CHCH_3NH_3)_2PbI_4$, (R = CH_3, Cl). *Acs. Omega* **2019**, *4*, 19565−19572.
(21) Adnan, M.; Baumberg, J. J.; Vijaya Prakash, G Linear and Nonlinear Optical Probing of Various Excitons in 2D Inorganic-Organic Hybrid Structures. *Sci. Rep.* **2020**, *10*, 2615.
(22) Gautier, R.; Paris, M.; Massuyeau, F. Exciton Self-Trapping in Hybrid Lead Halides: Role of Halogen. *J. Am. Chem. Soc.* **2019**, *141*, 12619−12623.
(23) Nazarenko, O.; Kotyrba, M. R.; Yakunin, S.; Aebli, M.; Raino, G.; Benin, B. M.; Wörle, M.; Kovalenko, M. V. Guanidinium-Formamidinium Lead Iodide: A Layered Perovskite-Related Compound with Red Luminescence at Room Temperature. *J. Am. Chem. Soc.* **2018**, *140*, 3850−3853.
(24) Mao, L.; Wu, Y.; Stoumpos, C. C.; Wasielewski, M. R.; Kanatzidis, M. G. White-Light Emission and Structural Distortion in New Corrugated Two-Dimensional Lead Bromide Perovskites. *J. Am. Chem. Soc.* **2017**, *139*, 5210−5215.
(25) Barman, S.; Venkataraman, N. V.; Vasudevan, S.; Seshadri, R. Phase Transitions in the Anchored Organic Bilayers of Long-Chain Alkylammonium Lead Iodides $(C_nH_{2n+1}NH_3)_2PbI_4$; n = 12, 16, 18. *J. Phys. Chem. B* **2003**, *107*, 1875−1883.
(26) Billing, D. G.; Lemmerer, A. Synthesis, Characterization and Phase Transitions of the Organic-Inorganic Layered Perovskite-Type Hybrids $[(C_nH_{2n+1}NH_3)_2PbI_4$ (n= 12, 14, 16 and 18). *New J. Chem.* **2008**, *32*, 1736−1746.
(27) Pradeesh, K.; Baumberg, J. J.; Prakash, G. V. Temperature-induced exciton switching in long alkyl chain based inorganic-organic hybrids. *J. Appl. Phys.* **2012**, *111*, 013511.
(28) Han, X.; Zheng, Y.; Chai, S.; Chen, S.; Xu, J. 2d Organic-Inorganic Hybrid Perovskite Materials for Nonlinear Optics. *Nanophotonics* **2020**, *9* (7), 1787−1810.
(29) Ye, H.-Y.; Liao, W.-Q.; Hu, C.-L.; Zhang, Y.; You, Y.-M.; Mao, J.-G.; Li, P.-F.; Xiong, R.-G. Bandgap Engineering of Lead-Halide Perovskite-Type Ferroelectrics. *Adv. Mater.* **2016**, *28* (13), 2579−2586.
(30) Chen, X.-G.; Song, X.-J.; Zhang, Z.-X.; Li, P.-F.; Ge, J.-Z.; Tang, Y.-Y.; Gao, J.-X.; Zhang, W.-Y.; Fu, D.-W.; You, Y.-M.; Xiong, R.-G. Two-Dimensional Layered Perovskite Ferroelectric with Giant Piezoelectric Voltage Coefficient. *J. Am. Chem. Soc.* **2020**, *142* (2), 1077−1082.
(31) Ji, C.; Dey, D.; Peng, Y.; Liu, X.; Li, L.; Luo, J. Ferroelectricity-Driven Self-Powered Ultraviolet Photodetection with Strong Polarization Sensitivity in a Two-Dimensional Halide Hybrid Perovskite. *Angew. Chem., Int. Ed.* **2020**, *59* (43), 18933−18937.
(32) Mączka, M.; Gągor, A.; Ptak, M.; Paraguassu, W.; da Silva, T. A.; Sieradzki, A.; Pikul, A. Phase Transitions and Coexistence of Magnetic and Electric Orders in the Methylhydrazinium Metal Formate Frameworks. *Chem. Mater.* **2017**, *29* (5), 2264−2275.
(33) Liao, W.-Q.; Zhang, Y.; Hu, C.-L.; Mao, J.-G.; Ye, H.-Y.; Li, P.-F.; Huang, S. D.; Xiong, R.-G. A Lead-Halide Perovskite Molecular Ferroelectric Semiconductor. *Nat. Commun.* **2015**, *6*, 7338−7338.
(34) Ji, C.; Wang, S.; Li, L.; Sun, Z.; Hong, M.; Luo, J. The First 2D Hybrid Perovskite Ferroelectric Showing Broadband White-Light Emission with High Color Rendering Index. *Adv. Funct. Mater.* **2019**, *29*, 1805038.
(35) Yangui, A.; Garrot, D.; Lauret, J. S.; Lusson, A.; Bouchez, G.; Deleporte, E.; Pillet, S.; Bendeif, E. E.; Castro, M.; Triki, S.; Abid, Y.; Boukheddaden, K. Optical Investigation of Broadband White-Light Emission in Self-Assembled Organic-Inorganic Perovskite $(C_6H_{11}NH_3)_2PbBr_4$. *J. Phys. Chem. C* **2015**, *119* (41), 23638−23647.
(36) Jung, M.-H. White-Light Emission from the Structural Distortion Induced by Control of Halide Composition of Two-Dimensional Perovskites $((C_6H_5CH_2NH_3)_2PbBr_{4-x}Cl_x)$. *Inorg. Chem.* **2019**, *58* (10), 6748−6757.
(37) Saparov, B.; Mitzi, D. B. Organic-Inorganic Perovskites: Structural Versatility for Functional Materials Design. *Chem. Rev.* **2016**, *116* (7), 4558−4596.
(38) Mączka, M.; Ptak, M. Simple, Fast and Non-Destructive Method for Detection of Dimethylammonium Impurity in Photovoltaic Methylammonium Lead Halides. *Appl. Solid State Chem.* **2018**, *1*, 45−48.
(39) Wang, F.; Cao, Y.; Chen, C.; Chen, Q.; Wu, X.; Li, X.; Qin, T.; Huang, W. Materials toward the Upscaling of Perovskite Solar Cells: Progress, Challenges, and Strategies. *Adv. Funct. Mater.* **2018**, *28* (52), 1803753.
(40) Zhao, X.; Ng, J. D. A.; Friend, R. H.; Tan, Z.-K. Opportunities and Challenges in Perovskite Light-Emitting Devices. *ACS Photonics* **2018**, *5* (10), 3866−3875.
(41) Chouhan, L.; Ghimire, S.; Biju, V. Blinking Beats Bleaching: The Control of Superoxide Generation by Photo-Ionized Perovskite Nanocrystals. *Angew. Chem., Int. Ed.* **2019**, *58* (15), 4875−4879.
(42) Mączka, M.; Gagor, A.; Zaręba, J. K.; Stefanska, D.; Drozd, M.; Balciunas, S.; Simėnas, M.; Banys, J.; Sieradzki, A. Three-Dimensional Perovskite Methylhydrazinium Lead Chloride with Two Polar Phases and Unusual Second-Harmonic Generation Bistability above Room Temperature. *Chem. Mater.* **2020**, *32* (9), 4072−4082.
(43) Mączka, M. a.; Ptak, M.; Gagor, A.; Stefańska, D.; Zaręba, J. K.; Sieradzki, A. Methylhydrazinium Lead Bromide: Noncentrosymmetric Three-Dimensional Perovskite with Exceptionally Large Framework Distortion and Green Photoluminescence. *Chem. Mater.* **2020**, *32* (4), 1667−1673.
(44) Delil, A. A. M. Characterisation of the Dielectric Properties of the Propellants MON & MMH. In *AIP Conference Proceedings*, Albuquerque, NM, USA, Jan 15, 1998; El-Genk, M. S., Bragg, M. J., Eds.; AIP Publishing: College Park, MD, USA, 1998; Vol. *420*, p 258.
(45) Fleet, M. E. Distortion Parameters for Coordination Polyhedra. *Mineral. Mag.* **1976**, *40* (313), 531−533.
(46) Nazarenko, O.; Kotyrba, M. R.; Wörle, M.; Cuervo-Reyes, E.; Yakunin, S.; Kovalenko, M. V. Luminescent and Photoconductive Layered Lead Halide Perovskite Compounds Comprising Mixtures of Cesium and Guanidinium Cations. *Inorg. Chem.* **2017**, *56* (19), 11552−11564.
(47) Mercier, N.; Poiroux, S.; Riou, A.; Batail, P. Unique Hydrogen Bonding Correlating with a Reduced Band Gap and Phase Transition in

https://doi.org/10.1021/acs.chemmater.0c04440
Chem. Mater. XXXX, XXX, XXX−XXX

the Hybrid Perovskites $(HO(CH_2)_2NH_3)_2PbX_4$ (X = I, Br). *Inorg. Chem.* **2004**, *43* (26), 8361−8366.
(48) Samantaray, R.; Clark, R. J.; Choi, E. S.; Dalal, N. S. Elucidating the Mechanism of Multiferroicity in (NH4)3Cr(O2)4 and Its Tailoring by Alkali Metal Substitution. *J. Am. Chem. Soc.* **2012**, *134* (38), 15953−15962.
(49) Mączka, M.; Sieradzki, A.; Bondzior, B.; Dereń, P.; Hanuza, J.; Hermanowicz, K. Effect of Aliovalent Doping on the Properties of Perovskite-Like Multiferroic Formates. *J. Mater. Chem. C* **2015**, *3* (36), 9337−9345.
(50) Han, S.; Liu, X.; Liu, Y.; Xu, Z.; Li, Y.; Hong, M.; Luo, J.; Sun, Z. High-Temperature Antiferroelectric of Lead Iodide Hybrid Perovskites. *J. Am. Chem. Soc.* **2019**, *141* (32), 12470−12474.
(51) Kubelka, P.; Munk, F. Ein Beitrag Zur Optik Der Farbanstriche. *Z. Technol. Phys.* **1931**, *12*, 593−601.
(52) Yangui, A.; Pillet, S.; Lusson, A.; Bendeif, E.-E.; Triki, S.; Abid, Y.; Boukheddaden, K. Control of the White-Light Emission in the Mixed Two-Dimensional Hybrid Perovskites (C6H11NH3)2[PbBr4xIx]. *J. Alloys Compd.* **2017**, *699*, 1122−1133.
(53) Smith, M. D.; Karunadasa, H. I. White-Light Emission from Layered Halide Perovskites. *Acc. Chem. Res.* **2018**, *51* (3), 619−627.
(54) Wang, S.; Yao, Y.; Kong, J.; Zhao, S.; Sun, Z.; Wu, Z.; Li, L.; Luo, J. Highly Efficient White-Light Emission in a Polar Two-Dimensional Hybrid Perovskite. *Chem. Commun.* **2018**, *54* (32), 4053−4056.
(55) Kurtz, S. K.; Perry, T. T. A Powder Technique for the Evaluation of Nonlinear Optical Materials. *J. Appl. Phys.* **1968**, *39* (8), 3798−3813.
(56) Stoumpos, C. C.; Cao, D. H.; Clark, D. J.; Young, J.; Rondinelli, J. M.; Jang, J. I.; Hupp, J. T.; Kanatzidis, M. G. Ruddlesden-Popper Hybrid Lead Iodide Perovskite 2d Homologous Semiconductors. *Chem. Mater.* **2016**, *28* (8), 2852−2867.
(57) Zhang, Q.; Solanki, A.; Parida, K.; Giovanni, D.; Li, M.; Jansen, T. L. C.; Pshenichnikov, M. S.; Sum, T. C. Tunable Ferroelectricity in Ruddlesden-Popper Halide Perovskites. *ACS Appl. Mater. Interfaces* **2019**, *11* (14), 13523−13532.
(58) Chen, W.; Bhaumik, S.; Veldhuis, S. A.; Xing, G.; Xu, Q.; Grätzel, M.; Mhaisalkar, S.; Mathews, N.; Sum, T. C. Giant Five-Photon Absorption from Multidimensional Core-Shell Halide Perovskite Colloidal Nanocrystals. *Nat. Commun.* **2017**, *8*, 15198.
(59) Medishetty, R.; Zaręba, J. K.; Mayer, D.; Samoć, M.; Fischer, R. A. Nonlinear Optical Properties, Upconversion and Lasing in Metal-Organic Frameworks. *Chem. Soc. Rev.* **2017**, *46* (16), 4976−5004.
(60) Schwich, T.; Cifuentes, M. P.; Gugger, P. A.; Samoc, M.; Humphrey, M. G. Electronic, Molecular Weight, Molecular Volume, and Financial Cost-Scaling and Comparison of Two-Photon Absorption Efficiency in Disparate Molecules (Organometallic Complexes for Nonlinear Optics. 48.) - a Response to "Comment on 'Organometallic Complexes. *Adv. Mater.* **2011**, *23* (12), 1433−1435.
(61) Samoc, M.; Matczyszyn, K.; Nyk, M.; Olesiak-Banska, J.; Wawrzynczyk, D.; Hanczyc, P.; Szeremeta, J.; Wielgus, M.; Gordel, M.; Mazur, L.; Kolkowski, R.; Straszak, B.; Cifuentes, M. P.; Humphrey, M. G. Nonlinear Absorption and Nonlinear Refraction: Maximizing the Merit Factors. In *Organic Photonic Materials and Devices XIV, Proceedings of the SPIE*, San Francisco, CA, USA, Jan 21−26, 2012; Tabor, C., Kajzar, F., Kaino, T., Koike, Y., Eds.; SPIE: Bellingham, WA, USA, 2012; Vol. *8258*, p 82580V.
(62) Olesiak-Banska, J.; Gordel, M.; Kolkowski, R.; Matczyszyn, K.; Samoc, M. Third-Order Nonlinear Optical Properties of Colloidal Gold Nanorods. *J. Phys. Chem. C* **2012**, *116* (25), 13731−13737.
(63) Gordel, M.; Olesiak-Banska, J.; Kolkowski, R.; Matczyszyn, K.; Buckle, M.; Samoc, M. Shell-Thickness-Dependent Nonlinear Optical Properties of Colloidal Gold Nanoshells. *J. Mater. Chem. C* **2014**, *2* (35), 7239−7246.
(64) Sheldrick, G. M. Crystal Structure Refinement with Shelxl. *Acta Crystallogr., Sect. C: Struct. Chem.* **2015**, *71*, 3−8.
(65) Glazer, A. M.; Lewis, J. G.; Kaminsky, W. An Automatic Optical Imaging System for Birefringent Media. *Proc. R. Soc. London, Ser. A* **1996**, *452* (1955), 2751−2765.
(66) Geday, M. A.; Kaminsky, W.; Lewis, J. G.; Glazer, A. M. Images of Absolute Retardance L. Deltan, Using the Rotating Polariser Method. *J. Microsc.* **2000**, *198* (1), 1−9.
(67) Roleder, K. Measurements of the High-Temperature Electrostrictive Properties of Ferroelectrics. *J. Phys. E: Sci. Instrum.* **1983**, *16* (12), 1157−1159.

https://doi.org/10.1021/acs.chemmater.0c04440
Chem. Mater. XXXX, XXX, XXX−XXX